A laser-driven droplet source for plasma physics applications

Bastian Aurand[1] 🄳, Esin Aktan[1], Kerstin Maria Schwind[1], Rajendra Prasad[1], Mirela Cerchez[1], Toma Toncian[2] and Oswald Willi[1]

[1]Institut für Laser- und Plasmaphysik, Heinrich-Heine-Universität Düsseldorf, D-40225 Düsseldorf, Germany and [2]Institute for Radiation Physics, Helmholtz-Zentrum Dresden-Rossendorf, 01328 Dresden, Germany

Abstract

In this paper, we report on the acceleration of protons and oxygen ions from tens of micrometer large water droplets by a high-intensity laser in the range of 10^{20} W/cm^2. Proton energies of up to 6 MeV were obtained from a hybrid acceleration regime between classical Coulomb explosion and shocks. Besides the known thermal energy spectrum, a collective acceleration of oxygen ions of different charge states is observed. 3D PIC simulations and analytical models are employed to support the experiential findings and reveal the potential for further applications and studies.

Introduction

The acceleration of charged particles in laser-plasma interactions was demonstrated more than 20 years ago, by Coulomb-exploding small molecular clusters (Ditmire *et al.*, 1996, 1999) resulting in a spatial more or less isotropic acceleration of ions. When in the early 2000s, first experiments revealed the capability of ion acceleration from solid targets (Clark *et al.*, 2000; Snavely *et al.*, 2000), the effect of target-normal-sheath acceleration (TNSA) (Wilks *et al.*, 2001; Mora, 2003) gained a high interest and moved the scope of research onto studying a wide range of parameter dependence, for example, pulse duration, target thickness, or laser-energy dependence. More recently, other acceleration mechanisms, like radiation-pressure acceleration (RPA; Henig *et al.*, 2009; Yan *et al.*, 2009; Aurand *et al.*, 2013) or break-out-afterburner (BOA; Yin *et al.*, 2006) were intensively studied. All those effects use solid targets which come with certain drawbacks, like the need of target replacement after every shot and, in most cases, a high debris and shrapnel production, damaging optics and degrading the laser beam quality over time.

In a recent experiment, we demonstrated the stable multi-Hertz acceleration (Aurand *et al.*, 2019) of protons from tens of nanometer large cryogenic hydrogen clusters (Grieser *et al.*, 2019), an alternative target, overcoming some of the aforementioned problems. In this Coulomb-explosion driven scheme, proton energies in the range of hundreds of keV were obtained in a spatially isotropic distribution around the interaction point. The low particle energy compared to experiments, for example, using foil targets is a result of the cluster size and can be overcome by larger clusters, generated for example with different cluster source setting. Developing a new cluster source, the cluster size was increased to the 10 s on micrometer range, with the drawback of a very low interaction probability with these large clusters (Aurand *et al.*, 2020). Another disadvantage of experiments using the cryogenic equipment comes with restrictions on the accessibility of the interaction chamber due to warm-up and cool-down times, which are typically in the order of several hours. A different approach to generate mass-limited targets is the use of liquids which can be either dispersed as a spray (Ramakrishna *et al.*, 2010; Prasad *et al.*, 2012) generating nanometer-size particles or as a continuous train of droplets (Schnuerer *et al.*, 2005; Sokollik *et al.*, 2009). While in the previous experiments rather small droplets in the range of 16-μm diameter were used to investigated the plasma and electric field formation (Sokollik *et al.*, 2009), we were particular interested in larger droplets in the order of 50 μm diameter to study, if a further increase in droplet target size results on an increase in particle energy. To our knowledge a similar target size was used in before by Burza *et al.* (2011), but the targets in this study were hollow shells, and the scope of the work presented was pointing toward an energy enhancement due to the special geometry. In this manuscript, we report on the results of the laser interacting with water droplets in the order of 50-μm diameter. The acceleration of protons, the resulting proton beam profile, and the effect of the target geometry on the electron motion for purely mass-limited targets compared to a two-dimensional target structure were studied.

CAMBRIDGE
UNIVERSITY PRESS
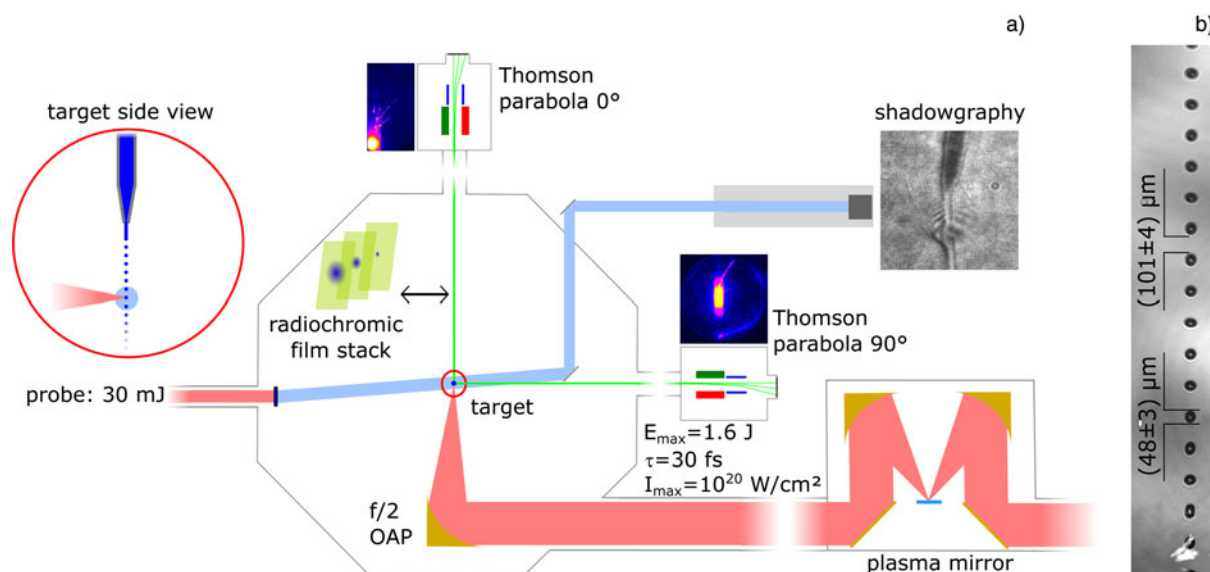
Fig. 1. (a) Scheme of the experimental setup. An f/2-OAP focussed the pump -pulse onto the droplet beam. The ion spectrum was measured in 0° and 90° with respect to the incident pump-beam axis. Additional RCF stacks could be placed in the forward direction. For alignment purpose and to measure the plasma expansion velocity, a frequency-doubled probe-beam is used to perform shadowgraphy. (b) Shadowgraphy image of the droplet stream.

Setup

The droplet target generator is based on a reservoir from which a liquid – here water – is pressed by a backing gas into a glass capillary. Those capillaries were produced using a laser-heated fully automated capillary-puller to obtain reproducible results. In front of the capillary, a filter frit with a mesh size of $0.3\,\mu m$ was implemented to prevent clogging of any residual particles in the nozzle tip. Careful handling and pre-cleaning, as well as the use of ultra-pure water (HPLC grade) as droplet forming material lead to a continuous operation time of the capillary in the range of several hours in the experiment. The liquid exits the fine tip as continuous beam and breaks due to Plateau–Rayleigh Instabilities (Plateau, 1873; Rayleigh, 1878) into random fragments, which form droplets to minimize the surface energy. A piezo-actuator was attached to the capillary and excited at a multiple of the systems resonance frequency. These vibrations triggered the breakup and lead to a continuous formation of droplets of equal size and equal spacing. The technical details on the droplet target generator, like the parameter range and the dependence of the resulting capillary geometry on the pulling parameters, can be found in the publication by Schwind *et al.* (2019*a*). To control the droplet formations and as a diagnostic tool in the experiment, shadowgraphy was performed, using a frequency-doubled ($\lambda = 400\,nm$, $\tau = 30\,fs$) probe beam at an angle of 100° with respect to the pump-beam direction. A separate delay line enabled us to probe the interaction at different times in the range of several 100 s of picoseconds with respect to the arrival of the pump pulse. Figure 1b shows a shadowgraphy image of the droplets by this beam. The droplet size was estimated to $(48 \pm 3)\,\mu m$ and the spacing in between droplets about $(101 \pm 4)\,\mu m$.

The main setup is shown in Figure 1a. Using the ARCTURUS laser system at the University of Duesseldorf (Willi *et al.*, 2009), a 200 TW double CPA scheme Ti:sapphire laser with an XPW contrast enhancement unit. The laser pulse with up to 1.6 J of energy on target and a pulse duration of 30 fs was focused by an off-axis parabolic mirror (OAP) onto the droplet stream, which was sent vertically – top to bottom – through the interaction chamber. The

interaction point was set 15 mm downstream of the capillary tip, to prevent damage on the capillary. A focus diameter of $5\,\mu m$ (FWHM) was obtained, corresponding to an intensity of $1 \times 10^{20}\,W/cm^2$. Performing a long-term pointing stability test, we measured the drift of the focus position to be $(2.1 \pm 3.1)\,\mu m$ over 30 min. The proton energy spectra were measured simultaneously by two Thomson-parabola (TP) spectrometers (Gwynne *et al.*, 2014) in 0° and 90° with respect to the incident pump-beam axis. Using micro-channel plates (MCP) and a read out by CCD cameras enabled online monitoring of the spectrum. The energy resolution was chosen to be in the range of 0.05–10 MeV/n. Additional radiochromic films (RCF; Hey *et al.*, 2008) could be inserted in the laser forward direction to retrieve the spatially resolved proton beam profile in this direction.

Measurements

The effect of the mass limitation and the electrical insulation of the droplets compared to the jet was studied. Therefore, the target expansion was probed for two different cases. Besides shooting on the isolated droplets, the interaction point was moved closer to the capillary nozzle to interact with the water jet before its fragments. This case represents a two-dimensional target structure, allowing hot electrons to escape along the jet direction. Figure 2a and 2b shows the raw images of the shadowgraphy for the laser, interacting with the jet before fragmentation and interaction with the droplets for a time in between 0 and 750 ps after the main pulse arrives, respectively. From those data, the longitudinal expansion velocity – full extension along the laser propagation direction – can be calculated to $(0.26 \pm 0.08)\,\mu m/ps$ for the jet and $(0.45 \pm 0.04)\,\mu m/ps$ in case of the droplets, as presented in Figure 2c. The difference by a factor of 1.6 can be correlated to the transverse escape of the electrons in the jet case, reducing the target heating and therefore the expansion velocity.

This escape of the electrons described above can be observed experimentally in the accelerated proton beam profile. Placing an RCF layer in the laser forward direction, measuring the spatial
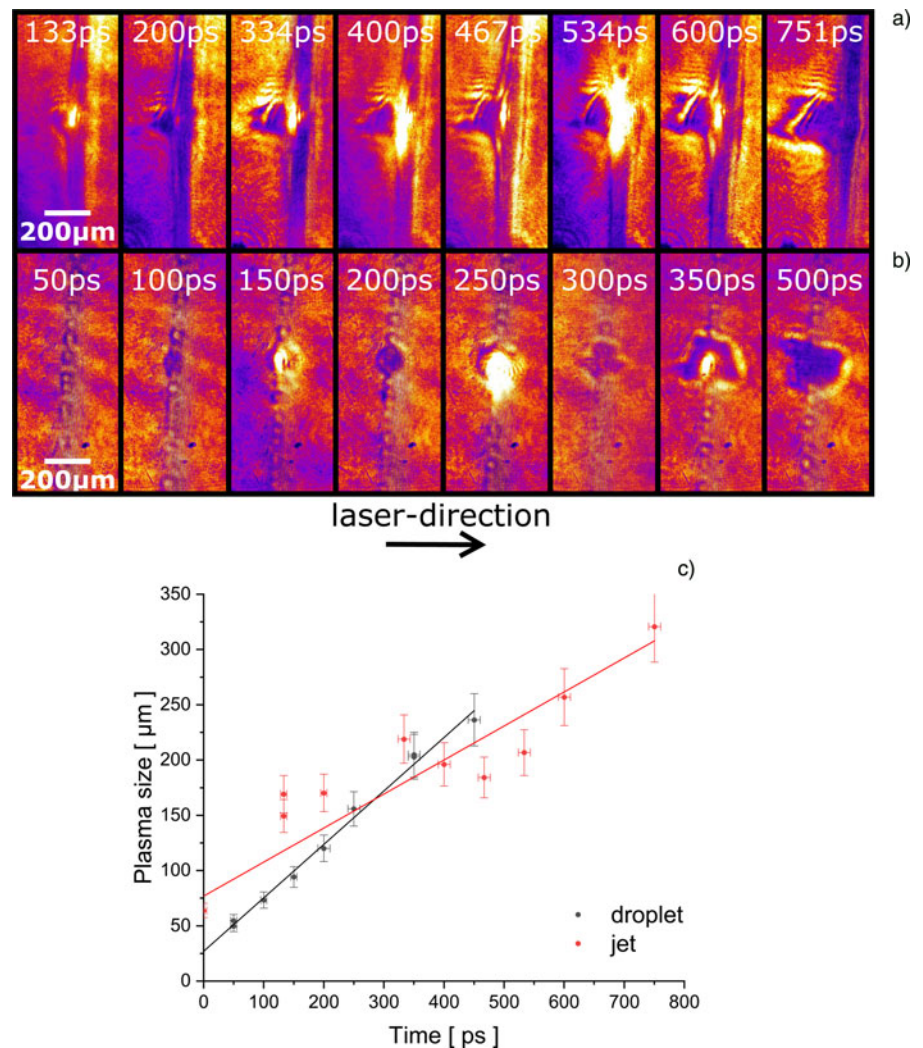
Fig. 2. (a,b) Shadowgraphy raw images of the plasma expansion from a water jet and droplets, probed at different delays in between 0 and 750 ps. (c) Measurement of the longitudinal expansion velocity of the jet or the droplet case, respectively.

beam profile of the protons ($1.0\,\text{MeV} < E_{\text{Kin}} < 1.3\,\text{MeV}$) as shown in Figure 3, reveals the differences for both cases. In the horizontal plane, the opening angle for the jet is $\Theta_{\text{h,jet}} > \pm 30°$ and for the droplet about $\Theta_{\text{h,drop}} = \pm 9°$. In the vertical plane, both opening angles are similar $\Theta_{\text{v,jet}} = \Theta_{\text{v,drop}} = \pm 8°$. This can be understood by accounting for the vertical escape of the electrons, which leads to a smoother electric field gradient in this direction compared to the horizontal plane. The proton divergence angle is proportional to the field gradient of the electric sheath field, as demonstrated before by Aurand *et al.* (2016) for a flat target, working with an elongated laser beam structure. In the present case, the strong gradient in the horizontal direction causes a high divergence of the proton beam in this direction, resulting in a line-shape structure. In the case of the droplet, the proton beam pattern is symmetric around the laser forward direction since the electrons heated in the target perform a homogeneous motion, for example, to compensate reflux-currents, along the droplet surface. For both conditions, a filamentation in the proton beam profile becomes visible, which was observed before for non-conducting target material, for example, by Antici *et al.* (2017). This can be explained by *Weibel instabilities* Weibel (1959), marking insufficient reflux of charges, causing a filamentation of the currents driven in the target, which imprints on the rear side sheath field and therefore on the proton beam profile.

Measuring the proton energy spectra simultaneously in 0° and 90° reveal more information on the acceleration process from the droplet target. As can be seen in Figure 4, protons are accelerated in both spatial directions. In the 90° direction, the energy distribution is continuous, similar to a Boltzmann-shaped thermal distribution occurring for TNSA with a maximum proton energy of up to 6 MeV. In the 0° direction, the particle flux is overall much weaker, showing dominant peaks toward the cutoff energy at around 1.5–2.0 MeV. This peaked proton spectra in 0° direction appeared for most of the shots, while for the remaining spectra, there is only the very weak tail, as for example visible in the raw data image of Figure 5, reaching to about the same energy.

While in the 90° direction, the proton signal was dominant showing no acceleration of oxygen ions, in the 0° direction on some of the shots up to three times ionized oxygen (O^{1+}, O^{2+}, and O^{3+}) ions were detected. These ions have more or less similar energy of about 0.11 MeV/n for all three charge states, as can be seen in Figure 5.

Simulations and analytic results

The target expansion velocity measured for the droplet – as a mass-limited target – of $v_{\text{D}} = (0.45 \pm 0.04)\,\mu\text{m/ps}$ at an intensity
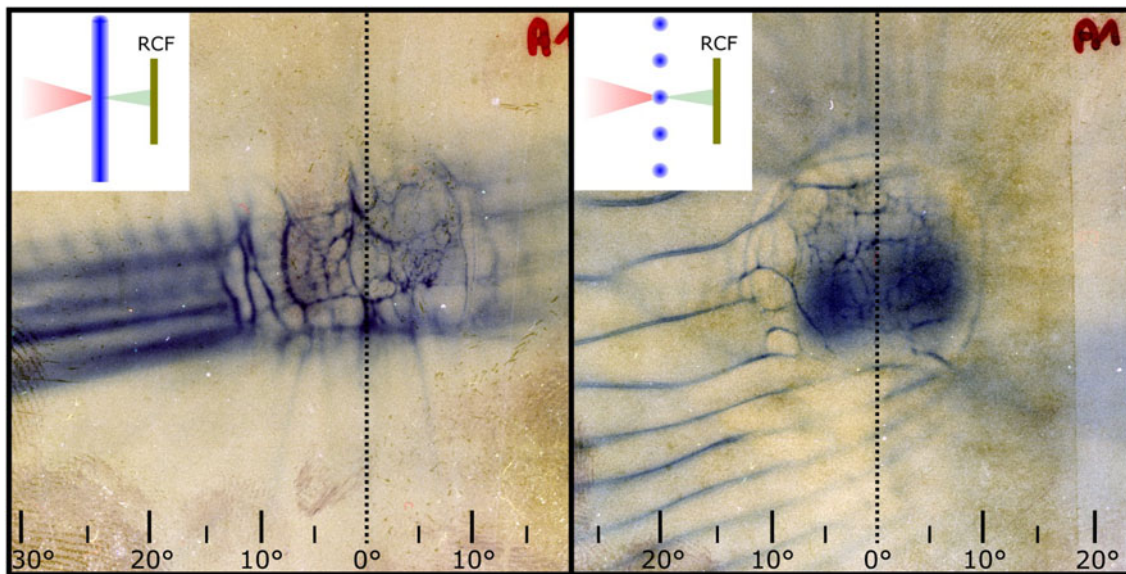
Fig. 3. Single layer of RCF placed 5 cm behind the interaction point in the forward direction. (Left) Interaction with the 2D jet structure leads to a directional proton beam signal, while (right) the interaction with a droplet gives a more homogeneous proton beam pattern.
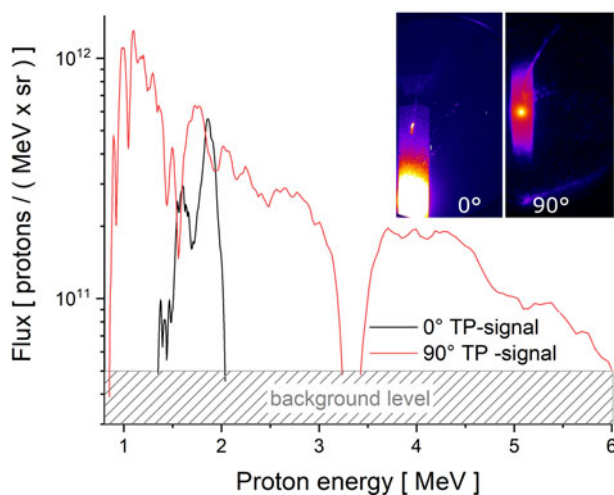
Fig. 4. Proton energy spectra measured in the 0° and 90° direction with respect to the laser axis from the droplet target.
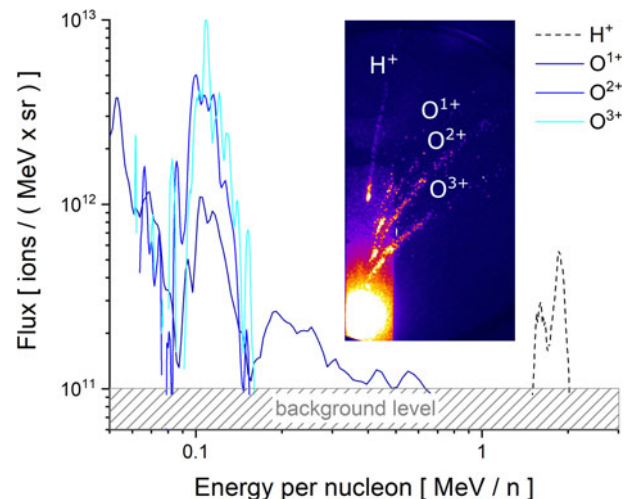
Fig. 5. Collective acceleration of protons and oxygen ions in the 0° direction with respect to the target occurring in some shots.

of 10^{20} W/cm^2 can be compared to previous measurements done on water droplet targets. Prasad *et al.* (2011) revealed an expansion speed of 0.12 µm/ps for $I = 10^{18}$ W/cm^2 by inteferometric measurements, while Brandstätter *et al.* (2018) retrieved 0.02 µm/ps for a much lower intensity of $I = 10^{11}$ W/cm^2 using a time-of-flight (ToF) detector. Since the target volume in these cases is still small – in the order of a few hundred µm^3 – in a first approximation the droplet expansion velocity v_D can be used as the lower estimate for the plasma expansion velocity v_P. Using the correlation

$$T_e(v_P) = \frac{v_P^2 \cdot m_I}{Z_I} \qquad (1)$$

the electron temperature can be deduced to $T_e \approx 25$ keV for the assumption that the target is evenly heated. As already can be

seen in the raw images (Fig. 2), the expansion is not homogeneous, indicating that the heating and, therefore, the electron temperature is not evenly within the target, which will be further discussed in the simulation below. Therefore, the temperature above can only be used as a lower estimate of the achieved electron temperature.

Comparing the proton energy achieved (see Fig. 4) of 6 MeV to the other experiments on a spray or droplets, we got an increase in proton energy. In the spray experiments (Ramakrishna *et al.*, 2010; Prasad *et al.*, 2012) with a typical target size in the several 100 s of nanometer-diameter range proton energies of 1–2 MeV were obtained, while using droplets in the 10–20 µm diameter range, energies of 0.5–2 MeV were measured. With the specially designed 50 µm target in Burza *et al.* (2011), similar proton energies of 5–6 MeV were detected. It should be noted, using a 6-µm Ti-foil target and similar interaction conditions at the
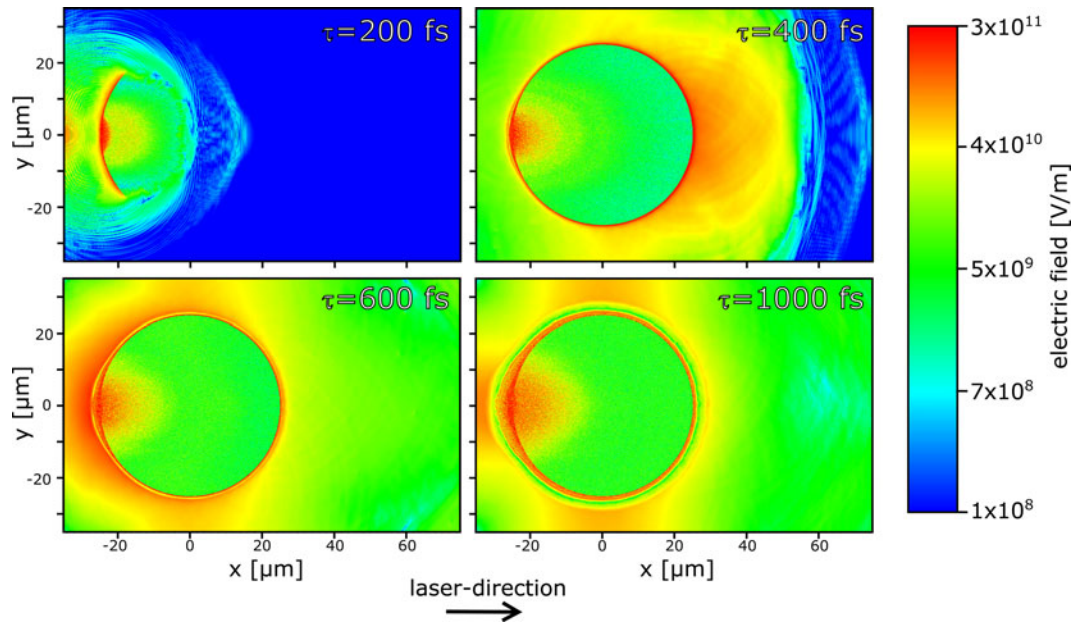
Fig. 6. Evolution of the electric field in the y-direction around the target in the center plane ($z = 0$) of the sphere at four different time steps after the interaction. An inhomogeneous field distribution around the sphere can be seen.

ARCTURUS laser system, a maximum proton energy of 6 MeV was reported in Schwind *et al.* (2019*b*).

In order to understand more details of the acceleration process, we performed 2D particle-in-cell (PIC) simulations, employing the EPOCH code (Arber *et al.*, 2017). The target was initialized as a sphere with a diameter of 48 µm and an initial density of 3×10^{22} atoms/cm^3, with a mass ratio of 0.811:0.189 (m_O/m_{H_2}). As starting condition every cell contained 100 neutral particles representing the hydrogen and 50 neutral particles representing the oxygen atoms, while the barrier-suppression tunnel-ionization model used by the code was employed to depict the ionization process. The laser pulse is represented by a Gaussian-shaped electromagnetic field, polarized in the y-direction, with a wavelength of $\lambda = 800$ nm propagating in the positive x-direction. The pulse is focused to a spot diameter of 4 µm and an intensity of 5×10^{19} W/cm^2 at the left surface of the sphere. Figure 6 shows the evolution of the electric field within the first picosecond after the interaction, for the central plane ($z = 0$) of the sphere. At $t = 0$, the pulse is initialized at the left boundary of the box. From the simulation can be seen, that at the time step of 200 fs, the laser pulse is already gone and a number of hot electrons generated at the target front are moving toward the target rear-surface. While a few of those hot electrons are capable to leave the target rear side – visible at the right edge of the simulation box for $\tau = 400$ fs – causing at this time a stronger electric field at the rear surface, a re-circulation of electrons around the target starts. At the time step of, for example, $\tau = 600$ fs, the field maximum is at the target front surface again and was observed to travel at least two times forth and back along the surface, while continuously decaying. This re-circulation of the electrons was observed for different target geometries, for example, by Quinn *et al.* (2011) for several hundred micrometer-thick plastic foils or by Tresca *et al.* (2011) for the case of mass-limited metal foils. Besides re-circulation, a more pronounced, quasi-static field evolves transverse to the laser propagation direction, which becomes visible at $\tau = 600$ fs and $\tau = 1000$ fs.

The investigation of ions accelerated from the target in the 0° and 90° directions (Fig. 7) with respect to the laser propagation direction show that the protons which are accelerated in the transverse direction (90°) achieve higher energy compared to those accelerated in the forward direction (0°). Comparing the timing in Figures 5 and 6, this energy increase is correlated to the appearance of the field enhancement in the transverse direction. Note that the chosen simulation period of 1 ps was a compromise between accuracy and simulation-runtime since the given geometry is already very large to model for with PIC code. Actually, the obtained proton energy is still increasing for both directions at the end of the simulation period. Nevertheless, the effect of directionality becomes visible.

While in our studies on the much smaller hydrogen clusters, the laser electric field removed all electrons quasi-instantaneously, resulting in an isotropic electrostatic repulsion of the remaining ions in a CE (Aurand *et al.*, 2019), the experimental and numerical results above reveal, on the one hand, that the laser cannot remove all electrons and, on the other hand, the acceleration process is not isotropic.

Assuming in a first approximation still a CE, for which only a portion $\hat{N}$ of the particles are ionized (assume $q_1 = 1$) and homogeneously distributed in the droplet, the electric potential $\Phi(r)$ at a position r can be described by

$$\Phi(r) = \frac{\hat{N}q_1}{4\pi\epsilon_0 R}\left(\frac{3}{2} - \frac{r^2}{2R^2}\right) \tag{2}$$

with R the droplet radius. The highest energy is gained by a proton of charge $q_2 = 1$ situated at the shell ($r = R$) of the sphere and is given by

$$E_{max} = \Phi(R, q_1) \cdot q_2 = \frac{\hat{N}q_1 q_2}{4\pi\epsilon_0 R} \tag{3}$$

The number $\hat{N}$ of ionized particles for such a large droplet is estimated to be the number of hot electrons N_{he} generated in the
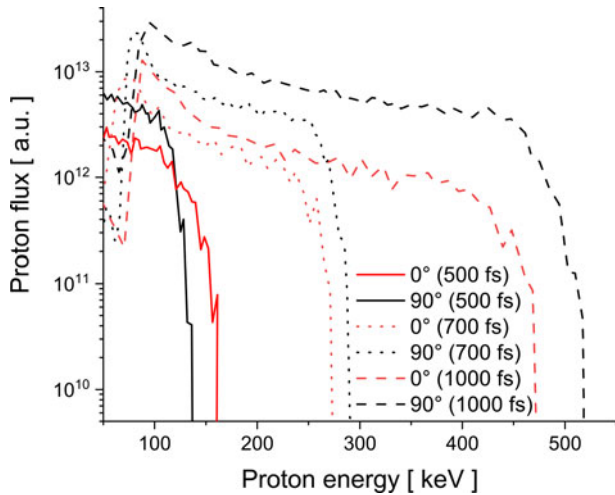
Fig. 7. Proton energy spectra obtained for the simulations within the first 1 ps after the laser-matter interaction in the 0° and 90° directions with respect to the laser propagation direction.

Fig. 8. Calculated maximum proton energies for a Coulomb explosion of water droplets depending on the size and the degree of ionization (solid lines) or the number of ionized particles calculated for the interaction (dashed line). The points represent the experimentally measured and numerical calculated maximum proton energies.

interaction, for example, employing the model of Andreev *et al.* (2004), with

$$N_{he} = \eta \frac{E_L}{T_{he}} \tag{4}$$

where η is the plasma absorption coefficient (Andreev *et al.*, 2003), $T_{he} = m_e c^2 (a_0 - 1)$ is the hot electron temperature (Wilks *et al.*, 2001), and E_L is the laser energy on target. In this simplified ansatz, it is assumed that the absorbed part of the laser energy is evenly distributed into a number of hot electrons with the temperature T_{he} derived from theory. For our interaction parameters with $I_L = 1 \times 10^{20}$ W/cm^2 and $E_L = 1.6$ J, we calculate $a_0 = 6.8$; $\eta = 0.23$; $T_{he} = 2.9$ MeV; and finally, $N_{he} \approx 1.2 \times 10^{12}$. Inserting this result in Eq. (3) would get maximum proton energy of $E_{max} = 69.8$ MeV which overestimates the measurement by a factor of 10. This discrepancy can be caused by different effect. Since the number of hot electrons (N_{he}) calculated above is only a fraction of $\approx 10^{-5}$ of all electrons in the droplet a strong interaction with the remaining cold electrons will occur, distributing the energy more evenly into a larger number of electrons, while at the same time, the neutral atoms will shield the electric fields. This is in agreement with the experimental finding that the electron temperature we found from the expansion measurement, assuming a fully homogenized temperature distribution is more than a factor of 10^3 smaller than the calculated one. In addition, the model as mentioned above does not include the effects by a multi-ion mixture as it is the case for water as a target material.

Figure 8 shows the maximum proton energy depending on the droplet size, comparing the numerical and analytical models and the experimental value. The solid black line marks the maximum achievable energy for the CE of a fully ionized water droplet with $q_1 = 10$ ($2 \cdot H^+ + O^{8+}$). As already deduced in the experiment, the highest ionization state observed for the oxygen ions is O^{3+}. For this reason, it can be assumed that the degree of ionization is less than 1, represented by the different ($\sigma_{ioniz.}$) of the target (colored solid lines in Fig. 8). Additionally, taking the number of electrons N_{he} [Eq. (4)] – the laser can heat/ionize directly for our interaction condition – as constant, is represented by the dashed line. Finally, the solid point denotes the experimental value and
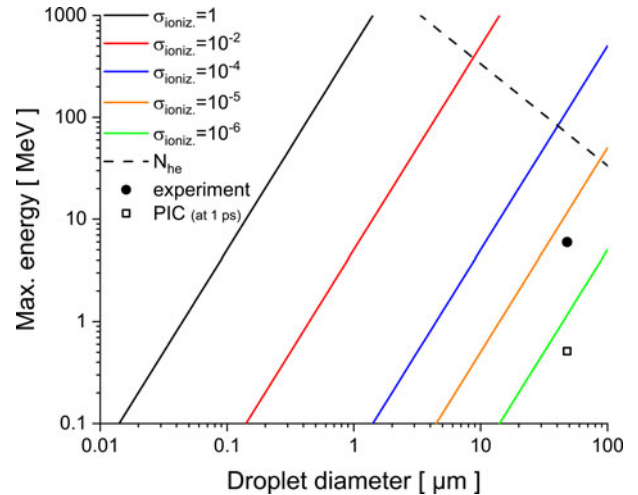
the hollow square the simulated value for the maximum proton energy after 1 ps into the simulation.

The effect of the mono-energetic ion components appearing in the 0° direction effect was observed before for different kinds of mass-limited targets. For heavy-water droplets, this effect was reported by Ter-Avetisyan *et al.* (2006) and for micrometer-size CH-dots attached to a Ti-foil by Schwoerer *et al.* (2006). A number of analytic models exist to explain this feature based on the target composition. While layered targets, with two spatially separated components, can be described by a model of Esirkepov *et al.* (2002), which is not suitable for our case, the model, proposed by Tikhonchuk *et al.* (2005) fits our experimental conditions. In this model, the ions are accelerated to a certain velocity by a shock, originating by a collisionless rarefaction, of light and heavy ions which are driven by a two-temperature electron distribution in the target. This is true for our experiment, in which the laser heats only a fraction of the target material, directly. The electrostatic potential due to the charge separation in the rarefaction is given by Ter-Avetisyan *et al.* (2006):

$$q\Phi = T_e (1 + \ln(8\sqrt{Z_i})) \tag{5}$$

with T_e the electron temperature and Z_i the heavy ion charge state. Assuming that the oxygen ions in the droplet bulk are at most one time ionized ($Z_i = 1$) and the electron temperature is between minimum 25 keV – as the lower estimate from the droplet expansion velocity above – and maximum 2.6 MeV – as calculated above –, this results in an electrostatic potential in between 77 kV and 9 MV accelerating the lighter ions (protons). This is in the range with the observed energy of 1.5–2 MeV for the protons in Figures 4 and 5. For the oxygen ions, as occurring in Figure 5, the acceleration process is not fully conclusive. While the normalized energy per nucleon, for $_1^1 H^+$ and $_8^{16} O^{1+}$, would indicate an acceleration in the same electrostatic field since the oxygen ions gains consequently about 1:16 of the energy per nucleon compared to the protons, the observation is not in agreement with the same energy measured for the different charge states of oxygen. If those different charge state ions are accelerated in the same field, they should gain different energies per nucleon. The

obtained results point toward a collective acceleration process, at least for the oxygen ions, which was observed for a mechanism like RPA (Aurand *et al.*, 2016) before. To our current understanding, there is no model explaining both features at the same time.

Conclusion

Employing a synchronized water droplet target generating droplets in the 50-µm diameter range, we investigated the interaction of these droplets with a high-intensity laser pulse, studying different effects. On the one hand, the benefit of mass-limited targets, compared to 2D target structures in terms of target heating, measured by the expansion velocity of the target, was found. On the other hand, a study on the spatial beam profile of the accelerated protons revealed that the target geometry can have a significant impact of the spatial distribution of these accelerated particles, for example, enabling a pre-shaping of the particle beam for further applications. Overall, proton energies of up to 6 MeV were obtained, which were higher compared to previous results, reported in the literature for smaller droplets and correspond to the proton energies obtained from foil targets using the same laser system. This underlines that this target scheme, with the benefits of high repetition rate and easy target delivery, in terms of energy is comparable to the results obtained by the well-known TNSA process. In addition, the energy spectra reveal – depending on the observation direction – a narrow energy distribution, which could be beneficial for further applications like post-acceleration. Employing numerical simulations enabled us to model the dependence of the acceleration process on the spatial direction and to identify a spatially inhomogeneous electrical field distribution evolving around the droplet as the cause. Different analytical models reveal that the achieved proton energies are within the expected range, depending on the number of hot electrons and their distribution within the target. The occurrence of the narrow-energetic spectral components for the protons can be explained by an existing model which accounts for the rarefaction of two ion species.

Besides the study of this fundamental processes, the droplet target source was proven to deliver a continuous stream of targets for the laser-plasma interaction and is capable to operate over several hours as a source for laser-accelerated protons in the MeV range.

References

Andreev AA, Platonov KYu, Okada T and Toraya S (2003) Nonlinear absorption of a short intense laser pulse in a nonuniform plasma. *Physics of Plasmas* **10**, 220–226.

Andreev AA, Okada T, Platonov KYu and Toraya S (2004) Parameters of a fast ion jet generated by an intense ultrashort laser pulse on an inhomogeneous plasma foil. *Laser and Particle Beams* **22**, 431–438.

Antici P, Boella E, Chen SN, Andrews DS, Barberio M, Boker J, Cardelli F, Feugeas JL, Glesser M, Nicolai P, Romagnani L, Sciscio M, Starodubtsev M, Willi O, Kieffer JC, Tikhonchuk V, Pepin H, Silva LO, Humieres E and Fuchs J (2017) Acceleration of collimated 45 MeV protons by collisionless shocks driven in low-density, large-scale gradient plasmas by a 1^{20} W/cm^2, 1 µm laser. *Nature Scientific Reports* **7**, 16463.

Arber TD, Bennett K, Brady CS, Lawrence-Douglas A, Ramsay MG, Sircombe NJ, Gillies P, Evans RG, Schmitz H, Bell AR and Ridgers CP (2017) Contemporary particle-in-cell approach to laser-plasma modelling. *Plasma Physics and Controlled Fusion* **57**, 113001.

Aurand B, Kuschel S, Jaeckel O, Roedel C, Zhao HY, Herzer S, Paz AE, Bierbach J, Polz J, Elkin B, Paulus GG, Karmakar A, Gibbon P, Kuehl T and Kaluza MC (2013) Radiation pressure-assisted acceleration of ions using multi-component foils in high-intensity laser-matter interactions. *New Journal of Physics* **15**, 033031.

Aurand B, Senje L, Svensson K, Hansson M, Higginson A, Gonoskovc A, Marklund M, Persson A, Lundh O, Neely D, McKenna P and Wahlstrom CG (2016) Manipulation of the spatial distribution of laser-accelerated proton beams by varying the laser intensity distribution. *Physics of Plasmas* **23**, 023113.

Aurand B, Grieser S, Toncian T, Aktan E, Cerchez M, Lessmann L, Prasad R, Khoukaz A and Willi O (2019) A multihertz, kiloelectronvolt pulsed proton source from a laser irradiated continuous hydrogen cluster target. *Physics of Plasmas* **26**, 073102.

Aurand B, Schwind KM, Toncian T, Aktan E, Cerchez M, Lessmann L, Mannweiler C, Prasad R, Khoukaz A and Willi O (2020) Study of the parameter dependence of laser-accelerated protons from a hydrogen cluster source. *New Journal of Physics* **22**, 033025.

Brandstätter M, Gambino N and Abhari RS (2018) Temporally and spatially resolved ion dynamics of droplet-based laser-produced tin plasmas in lateral expansion direction. *Journal of Applied Physics* **123**, 043308.

Burza M, Gonoskov A, Genoud G, Persson A, Svensson K, Quinn M, McKenna P, Marklund M and Wahlstrom CG (2011) Hollow microspheres as target. *New Journal of Physics* **23**, 013030.

Clark EL, Krushelnick K, Zepf M, Beg FN, Tatarakis M, Machacek A, Santala MI, Watts II, Norreys PA and Dangor AE (2000) Energetic heavy-Ion and proton generation from ultraintense laser-plasma interactions with solids. *Physical Review Letters* **85**, 1654–1661.

Ditmire T, Gumbrell ET, Smith RA, Mountford L and Hutchinson MH (1996) Supersonic ionization wave driven by radiation transport in a short-pulse laser-produced plasma. *Physical Review Letters* **77**, 498–501.

Ditmire T, Zweiback J, Yanovsky VP, Cowan TE, Hays G and Wharton KB (1999) Nuclear fusion from explosions of femtosecond laser-heated deuterium clusters. *Nature* **398**, 489–492.

Esirkepov TZh, Bulanov SV, Nishihara K, Tajima T, Pegoraro F, Khoroshkov VS, Mima K, Daido H, Kato Y, Kitagawa Y, Nagai K and Sakabe S (2002) Proposed double-layer target for the generation of high-quality laser-accelerated ion beams. *Physical Review Letters* **89**, 175003.

Grieser S, Aurand B, Aktan E, Bonaventura D, Buescher M, Cerchez M, Engin I, Leßmann L, Mannweiler C, Prasad R, Willi O and Khoukaz A (2019) Nm-sized cryogenic hydrogen clusters for a laser-driven proton source. *Review of Scientific Instruments* **90**, 043301.

Gwynne D, Kar S, Doria D, Ahmed H, Cerchez M, Fernandez J, Gray RJ, Green JS, Hanton F, MacLellan DA, McKenna P, Najmudin Z, Neely D, Ruiz JA, Schiavi A, Streeter M, Swantusch M, Willi O, Zepf M and Borghesi M (2014) Modified Thomson spectrometer design for high energy, multi-species ion sources. *Review of Scientific Instruments* **85**, 033304.

Henig A, Steinke S, Schnurer M, Sokollik T, Horlein R, Kiefer D, Jung D, Schreiber J, Hegelich BM, Yan XQ, Meyer-ter-Vehn J, Tajima T, Nickles PV, Sandner W and Habs D (2009) Radiation-pressure acceleration of ion beams driven by circularly polarized laser pulses. *Physical Review Letters* **103**, 245003.

Hey DS, Key MH, Mackinnon AJ, MacPhee AG, Patel PK, Freeman RR, Van Woerkom LD and Castaneda CM (2008) Use of GafChromic film to diagnose laser generated proton beams. *Review of Scientific Instruments* **79**, 053501.

Mora P (2003) Plasma expansion into a vacuum. *Physical Review Letters* **90**, 185002.

Plateau JAF (1873) *Statique expérimentale et théorique des liquides soumis aux seules forces moléculaires*. Paris: Gauthier-Villars.

Prasad YBSR, Barnwal S, Naik PA, Chakera JA and Gupta PD (2011) Chirped pulse interferometry for time resolved density and velocity

measurements of laser produced plasmas. *Journal of Applied Physics* **110**, 023305.

Prasad R, Borghesi M, Abicht F, Nickles PV, Stiel H, Schnurer M and Ter-Avetisyan S (2012) Ethanol (C_2H_5OH) spray of sub-micron droplets for laser driven negative ion source. *Review of Scientific Instruments* **83**, 083301.

Quinn MN, Yuan XH, Lin XX, Carroll DC, Tresca O, Gray RJ, Coury M, Li C, Li YT, Brenner CM, Robinson APL, Neely D, Zielbauer B, Aurand B, Fils J, Kuehl T and McKenna P (2011) Refluxing of fast electrons in solid targets irradiated by intense, picosecond laser pulses. *Plasma Physics and Controlled Fusion* **53**, 025007.

Ramakrishna B, Murakami M, Borghesi M, Ehrentraut L, Nickles PV, Schnuerer M, Steinke S, Psikal J, Tikhonchuk V and Ter-Avetisyan S (2010) Laser-driven quasimonoenergetic proton burst from water spray target. *Physics of Plasmas* **17**, 083113.

Rayleigh J (1878) On the instability of jets. *Proceedings of the London Mathematical Society* **10**, 4–13.

Schnuerer M, Ter-Avetisyan S, Busch S, Risse E, Kalachnikov MP, Sandner W and Nickles P (2005) Ion acceleration with ultrafast laser driven water droplets. *Laser and Particle Beams* **23**, 337–343.

Schwind KM, Aktan E, Cerchez M, Prasad R, Willi O and Aurand B (2019a) A high-repetition rate droplet-source for plasma physics applications. *Nuclear Instruments and Methods in Physics Research Section A* **928**, 65–69.

Schwind KM, Aktan E, Prasad R, Cerchez M, Eversheim D, Willi O and Aurand B (2019b) An online beam profiler for laser-accelerated protons. *Review of Scientific Instruments* **90**, 053307.

Schwoerer H, Pfotenhauer S, Jackel O, Amthor KU, Liesfeld B, Ziegler W, Sauerbrey R, Ledingham KW and Esirkepov T (2006) Laser-plasma acceleration of quasi-monoenergetic protons from microstructured targets. *Nature* **439**, 445–453.

Snavely RA, Key MH, Hatchett SP, Cowan TE, Roth M, Phillips TW, Stoyer MA, Henry EA, Sangster TC, Singh MS, Wilks SC, MacKinnon A, Offenberger A, Pennington DM, Yasuike K, Langdon AB, Lasinski BF, Johnson J, Perry MD and Campbell EM (2000) Intense high-energy proton beams from Petawatt-laser irradiation of solids. *Physical Review Letters* **85**, 2945–2953.

Sokollik T, Schnurer M, Steinke S, Nickles PV, Sandner W, Amin M, Toncian T, Willi O and Andreev AA (2009) Directional laser-driven ion acceleration from microspheres. *Physical Review Letters* **103**, 135003.

Ter-Avetisyan S, Schnurer M, Nickles PV, Kalashnikov M, Risse E, Sokollik T, Sandner W, Andreev A and Tikhonchuk V (2006) Quasimonoenergetic deuteron bursts produced by ultraintense laser pulses. *Physical Review Letters* **96**, 145006.

Tikhonchuk VT, Andreev AA, Bochkarev SG and Bychenkov VYu (2005) Ion acceleration in short-laser-pulse interaction with solid foils. *Plasma Physics and Controlled Fusion* **47**, B869–B877.

Tresca O, Carroll DC, Yuan XH, Aurand B, Bagnoud V, Brenner CM, Coury M, Fils J, Gray RJ, Kuehl T, Li C, Li YT, Lin XX, Quinn MN, Evans RG, Zielbauer B, Roth M, Neely D and McKenna P (2011) Controlling the properties of ultraintense laser-proton sources using transverse refluxing of hot electrons in shaped mass-limited targets. *Plasma Physics and Controlled Fusion* **53**, 105008.

Weibel ES (1959) Spontaneously growing transverse waves in a plasma due to an anisotropic velocity distribution. *Physical Review Letters* **2**, 83–84.

Wilks SC, Langdon AB, Cowan TE, Roth M, Singh M, Hatchett S, Key MH, Pennington D, MacKinnon A and Snavely RA (2001) Energetic proton generation in ultra-intense laser-solid interactions. *Physics of Plasmas* **8**, 542–549.

Willi O, Behmke M, Gezici L, Hidding B, Jung R, Koenigstein T, Pipahl A, Osterholz J, Pretzler G, Pukhov A, Toncian M, Toncian T, Heyer M, Jaeckel O, Kuebel M, Paulus G, Roedel C, Schlenvoigt HP, Ziegler W, Buescher M, Feyt A, Lehrach A, Ohm H, Oswald G, Raab N, Ruzzo M, Seltmann M and Zhang Q (2009) Particle and x-ray generation by irradiation of gaseous and solid targets with a 100 TW laser pulse. *Plasma Physics and Controlled Fusion* **51**, 124049.

Yan XQ, Lin C, Sheng ZM, Guo ZY, Liu BC, Lu YR, Fang JX and Chen JE (2009) Generating high-current monoenergetic proton beams by a circularly polarized laser pulse in the phase-stable acceleration regime. *Physical Review Letters* **13**, 135003.

Yin L, Albright BJ, Hegelich BM and Fernandez JC (2006) GeV laser ion acceleration from ultrathin targets: the laser break-out afterburner. *Laser and Particle Beams* **24**, 291–298.